Interrogating the Theranostic Capacity of a MUC16-Targeted Antibody for Ovarian Cancer

Kyeara N. Mack[1,2], Zachary V. Samuels[1], Lukas M. Carter[1], Tara D. Viray[1], Komal Mandleywala[1], Cory L. Brooks[3], Michael A. Hollingsworth[4], Prakash Radhakrishnan[4], and Jason S. Lewis[1,2,5]

[1]Department of Radiology, Memorial Sloan Kettering Cancer Center, New York, New York; [2]Department of Pharmacology, Weill Cornell Graduate School of Medical Sciences, Weill Cornell Medicine, New York, New York; [3]Department of Chemistry and Biochemistry, California State University, Fresno, California; [4]Eppley Institute for Research in Cancer and Allied Diseases, University of Nebraska Medical Center, Omaha, Nebraska; and [5]Molecular Pharmacology Program, Memorial Sloan Kettering Cancer Center, New York, New York

Aberrantly expressed glycans on mucins such as mucin-16 (MUC16) are implicated in the biology that promotes ovarian cancer (OC) malignancy. Here, we investigated the theranostic potential of a humanized antibody, huAR9.6, targeting fully glycosylated and hypoglycosylated MUC16 isoforms. **Methods:** In vitro and in vivo targeting of the diagnostic radiotracer [^{89}Zr]Zr-DFO-huAR9.6 was investigated via binding experiments, immuno-PET imaging, and biodistribution studies on OC mouse models. Ovarian xenografts were used to determine the safety and efficacy of the therapeutic version, [^{177}Lu]Lu-CHX-A″-DTPA-huAR9.6. **Results:** In vivo uptake of [^{89}Zr]Zr-DFO-huAR9.6 supported in vitro–determined expression levels: high uptake in OVCAR3 and OVCAR4 tumors, low uptake in OVCAR5 tumors, and no uptake in OVCAR8 tumors. Accordingly, [^{177}Lu]Lu-CHX-A″-DTPA-huAR9.6 displayed strong antitumor effects in the OVCAR3 model and improved overall survival in the OVCAR3 and OVCAR5 models in comparison to the saline control. Hematologic toxicity was transient in both models. **Conclusion:** PET imaging of OC xenografts showed that [^{89}Zr]Zr-DFO-huAR9.6 delineated MUC16 expression levels, which correlated with in vitro results. Additionally, we showed that [^{177}Lu]Lu-CHX-A″-DTPA-huAR9.6 displayed strong antitumor effects in highly MUC16-expressing tumors. These findings demonstrate great potential for ^{89}Zr- and ^{177}Lu-labeled huAR9.6 as theranostic tools for the diagnosis and treatment of OC.

Key Words: PET imaging; radioimmunotherapy; MUC16; huAR9.6; ovarian cancer

J Nucl Med 2024; 65:580–585
DOI: 10.2967/jnumed.123.266524

Ovarian cancer (OC) causes more deaths than any other gynecologic malignancy, with a 5-y survival rate below 30% for patients diagnosed at advanced stages (*1*,*2*). The current standard of care for OC consists of surgery followed by platinum-based chemotherapy; however, these methods have failed to increase overall survival rates in patients because of tumor recurrence and chemoresistance (*2*,*3*). Cancer antigen 125 (CA125)—an epitope on mucin-16 (MUC16)—is a common and widely used serum biomarker for OC diagnosis. However, serum CA125 levels do not sufficiently detect all occurrences of early-stage disease (*4*). Therefore, there is a critical need for both additional detection methods and new targeted therapies that can improve patient survival.

Among the factors contributing to the lethality of OC is the aberrant glycosylation of carbohydrate residues on mucins, which promote metastasis and reduce overall survival (*5*). Membrane-bound mucins with aberrantly expressed *O*-linked glycans are emerging as promising targets for OC diagnosis and treatment because they are expressed solely on epithelial cancer cells (*6*). Studies have shown that elevated levels of hypoglycosylated MUC16 isoforms in OC patients correlate with disease stage and tumor volume (TV) better than the CA125 epitope (*7*). Thus, hypoglycosylated MUC16 could be a potential target for tumor detection via immuno-PET imaging.

Immuno-PET imaging offers a noninvasive approach to OC detection because it combines the tumor-targeting specificity of antibodies with the high sensitivity of PET imaging (*8*). This approach was evaluated with huAR9.6—a humanized antibody that binds to hypoglycosylated residues on MUC16 (*9*). Our previous work validated huAR9.6 as an immuno-PET radiopharmaceutical for OC detection (*10*). Expanding on these findings, we sought to further develop a radiotheranostic system using ^{89}Zr-labeled huAR9.6 to diagnose—and ^{177}Lu-labeled huAR9.6 to subsequently treat—OC.^{89}Zr is a favorable positron-emitting radionuclide, as its half-life (3.3 d) complements the circulation half-life of full-length antibodies. ^{177}Lu is an ideal therapeutic β^--emitting radionuclide because of its favorable half-life (6.6 d) and short tissue penetration range (mean, 670 μm) relative to other β^--emitting radionuclides used in the clinic (*11*).

Clinical imaging for OC patients has largely focused on the OC125 murine antibody that binds to CA125 (*12–14*). However, radiolabeled OC125 demonstrated uptake in noncancerous tissues, thus limiting its specificity for the detection of OC lesions (*15–17*) while additionally causing human antimurine antibody responses, which increase off-target toxicities (*18–20*). We reasoned that a humanized antibody that binds to hypoglycosylated MUC16 isoforms will provide superior specificity for the detection and treatment of OC lesions while simultaneously overcoming the limitations of using murine antibodies in patients. Here, we present a promising radiotheranostic system to detect hypoglycosylated MUC16 and deliver therapeutic levels of radiation in human OC mouse models.

Received Aug. 11, 2023; revision accepted Jan. 29, 2024.
For correspondence or reprints, contact Jason S. Lewis (lewisj2@mskcc.org).
Published online Mar. 14, 2024.

MATERIALS AND METHODS

The supplemental materials (available at http://jnm.snmjournals.org) provide information on cell lines, quantitative real-time polymerase chain reaction, flow cytometry, antibody functionalization and radiolabeling, binding assays, serum stability, dosimetry, and immunohistochemistry.

Xenograft Models

All in vivo experiments were approved by the Research Animal Resource Center and Institutional Animal Care and Use Committee (approval 08-07-013) at Memorial Sloan Kettering. Seven- to 8-wk-old CRL:NU-*Foxn1*^{nu} (Nu/Nu; Charles River Laboratories) female mice were purchased. The animals were housed in ventilated cages and given food and water ad libitum. For PET imaging studies with [^{89}Zr]Zr-DFO-huAR9.6, 7- to 8-wk-old Nu/Nu mice were xenografted subcutaneously with OVCAR3, OVCAR4, OVCAR5, and OVCAR8 tumors. OVCAR3 tumors were induced on the right shoulder by injection of 10 million cells followed by another injection of 5 million cells 1 wk later in a 150-μL cell suspension of a 1:1 (v/v) mixture of fresh medium to BD Matrigel (BD Biosciences). OVCAR4, OVCAR5, and OVCAR8 tumors were induced on the right flank by injection of 5 million cells in a 150-μL cell suspension of a 1:1 (v/v) mixture of fresh medium to BD Matrigel. For therapy and biodistribution studies with [^{177}Lu]Lu-DTPA-huAR9.6, 7- to 8-wk-old B6;129-*Rag2*^{tm1Fwa} *IL2rg*^{tm1Rsky}/DwlHsd (R2G2; Envigo) female mice were purchased. OVCAR3, OVCAR5, and OVCAR8 tumors were induced on the right flank of R2G2 mice by injection of 5 million cells in a 100-μL cell suspension of a 1:1 (v/v) mixture of fresh medium to BD Matrigel. Subcutaneous xenografts were used for in vivo imaging and biodistribution studies when TV reached about 150–300 mm^3.

PET and SPECT Imaging

PET/CT images were acquired on an Inveon PET/CT scanner (Siemens Healthcare). For PET imaging studies, [^{89}Zr]Zr-DFO-huAR9.6 in 150 μL of Chelex (Bio-Rad)-treated phosphate-buffered saline was injected via the lateral tail vein into OVCAR3-, OVCAR4-, OVCAR5-, and OVCAR8-bearing mice. OVCAR3-bearing Nu/Nu mice (n = 4) were injected with 7.73 ± 0.34 MBq (20 μg), OVCAR4-bearing Nu/Nu mice (n = 3) were injected with 7.07 ± 0.19 MBq (20 μg), OVCAR5-bearing Nu/Nu mice (n = 4) were injected with 7.12 ± 0.18 MBq (20 μg), and OVCAR8-bearing Nu/Nu mice (n = 3) were injected with 8.58 ± 0.19 MBq (20 μg). Each tumor model was imaged in independent experiments. For PET imaging studies of recurrent OVCAR3 tumors (n = 3), R2G2 mice were injected with [^{89}Zr]Zr-DFO-huAR9.6 (20 μg, 7.62 ± 0.11 MBq). SPECT/CT images were acquired on a NanoSPECT (Siemens Healthcare). OVCAR3-bearing R2G2 mice (n = 4) with recurrent tumors were injected with a second dose of [^{177}Lu]Lu-DTPA-huAR9.6 (9.87 ± 0.47 MBq, 60 μg) in 150 μL of Chelex-treated phosphate-buffered saline. All image analysis was performed using VivoQuant analysis software (Invicro).

Ex Vivo Biodistribution

For each tumor model, ex vivo biodistribution analyses were performed on separate cohorts of xenografted mice that were administered [^{89}Zr]Zr-DFO-huAR9.6 or [^{177}Lu]Lu-DTPA-huAR9.6. After serial PET/CT imaging, 144-h terminal biodistribution studies were conducted on OVCAR3-, OVCAR4-, OVCAR5-, and OVCAR8-bearing Nu/Nu mice. For serial biodistribution studies with [^{89}Zr]Zr-DFO-huAR9.6 (3 μg), OVCAR3-bearing R2G2 mice were injected with 1.06 ± 0.11 MBq, OVCAR4-bearing Nu/Nu mice were injected with 1.11 ± 0.05 MBq, OVCAR5-bearing Nu/Nu mice were injected with 1.11 ± 0.05 MBq, and OVCAR8-bearing Nu/Nu mice were injected with 1.22 ± 0.05 MBq. In blockade cohorts, mice were injected with a mixture of [^{89}Zr]Zr-DFO-huAR9.6 and a 100-fold excess (mass) of unlabeled huAR9.6. For serial biodistribution studies with [^{177}Lu]Lu-CHX-A″-DTPA-huAR9.6 (3 μg), OVCAR3-bearing R2G2 mice were injected with 1.17 ± 0.08 MBq. Radiotracer injections (150 μL diluted with Chelex-treated phosphate-buffered saline) were administered via the lateral tail vein.

Radioimmunotherapy

All mice were administered 60 μg of [^{177}Lu]Lu-CHX-A″-DTPA-huAR9.6 for therapy studies. R2G2 mice bearing OVCAR3 tumors were separated into 3 cohorts for administration of 9.25 MBq (TV, 247.4 ± 128.70 mm^3; n = 15), 18.5 MBq (TV, 398.40 ± 135.10 mm^3; n = 5), or 27.75 MBq (TV, 356.05 ± 127.12 mm^3; n = 5) of [^{177}Lu]Lu-CHX-A″-DTPA-huAR9.6 to determine the most efficacious dose. Two additional cohorts were used as controls: saline (TV, 247.73 ± 157.65 mm^3; n = 10) and [^{177}Lu]Lu-CHX-A″-DTPA-IgG1 isotype control (9.25 MBq; TV, 186.36 ± 102.67 mm^3; n = 10). The average body weight for mice bearing OVCAR3 xenografts was 29.3 ± 3.1 g. R2G2 mice bearing OVCAR5 and OVCAR8 tumors were separated into 3 cohorts: saline (OVCAR5 TV, 146.78 ± 68.36 mm^3 [n = 10], and OVCAR8 TV, 184.66 ± 42.48 mm^3 [n = 5]), 9.25 MBq of [^{177}Lu]Lu-CHX-A″-DTPA-IgG1 isotype control (OVCAR5 TV, 184.66 ± 62.59 mm^3 [n = 10], and OVCAR8 TV, 207.52 ± 79.77 mm^3 [n = 5]), and 9.25 MBq of [^{177}Lu]Lu-CHX-A″-DTPA-huAR9.6 (OVCAR5 TV, 182.99 ± 94.71 mm^3 [n = 10], and OVCAR8 TV, 388.48 ± 118.91 [n = 5]). The average body weight was 22.0 ± 1.4 g for mice bearing OVCAR5 xenografts and 26.0 ± 1.6 g for mice bearing OVCAR8 xenografts. Tumor measurements were taken twice a week, and weekly blood draws were obtained for analysis on the element HT5 hematology analyzer (HESKA). The endpoints were a tumor size of more than 2,000 mm^3, tumor ulceration or necrosis, severe petechiae, and a 20% weight loss if food or fluid did not improve the health status of the animal after the start of weight loss. Mice whose weight decreased received supplemental DietGel (ClearH$_2$O). Vernier calipers were used to measure the tumor dimensions, and the following equation was used to calculate TV (mm)^3:

$$\mathrm{TV} = \left(\frac{4\pi}{3}\right)\left(\frac{\alpha}{2}\right)^2\left(\frac{b}{2}\right),$$

where α is the longest axis of the tumor (mm) and b is the axis perpendicular to the longest axis (mm).

Statistical Analysis

Statistical analyses were performed using GraphPad Prism, version 10. Unpaired, 2-tailed t tests were used to analyze cell-binding assays. A 1-way ANOVA was used for analysis of organ uptake in biodistribution experiments. A correction for multiple comparisons was performed using the Tukey–Kramer method. Analysis of survival experiments was performed via a log rank (Mantel–Cox) test. A P value of less than 0.05 was considered significant.

Data Availability

The data generated in this study are available on request from the corresponding author.

RESULTS

HuAR9.6 Can Delineate Varying MUC16 Expression Levels in OC

[^{89}Zr]Zr-DFO-huAR9.6 was synthesized with high radiochemical purity (>98%), high specific activity (~0.37 MBq/μg), and was shown to be stable in human serum (Supplemental Figs. 1, 2, 3A, and 3B) (*21*,*22*). To assess the in vitro binding of huAR9.6, we conducted radioligand bead–based (*23*), saturation-binding,

cell-binding, and flow cytometry assays. [^{89}Zr]Zr-DFO-huAR9.6 showed high and specific binding to MUC16 in the bead-based assay (Supplemental Fig. 3C) and bound to the highly MUC16-expressing OVCAR3 cells with high affinity (dissociation constant, 6.2 nM) (Supplemental Fig. 4). The cell-binding assay with OVCAR3 (MUC16-positive/high), OVCAR4 (MUC16-positive/high), OVCAR5 (MUC16-positive/low), and OVCAR8 (MUC16-negative) showed strong binding to OVCAR3 (~76%) and OVCAR4 (~75%), minimal binding to OVCAR5 (~20%), and no binding to OVCAR8 (Fig. 1A). Flow cytometry analysis with huAR9.6 correlated with cell-binding data showing high binding to OVCAR3 and OVCAR4, marginal binding to OVCAR5, and no binding to OVCAR8 (Fig. 1B; Supplemental Fig. 5). Additionally, we analyzed *MUC16* messenger RNA expression levels in each cell line via real-time polymerase chain reaction. The results demonstrated varying *MUC16* messenger RNA expression levels, with the highest messenger RNA expression seen in the OVCAR4 cell line (Supplemental Fig. 6). To further investigate the binding of huAR9.6, nude mice were xenografted with OVCAR3, OVCAR4, OVCAR5, or OVCAR8 subcutaneous tumors, and ex vivo immunohistochemical analysis on tissue slices from these tumors was performed. Staining with huAR9.6 confirmed high expression in OVCAR3 and OVCAR4, minimal expression in OVCAR5, and no expression in OVCAR8 (Fig. 1C).

Building on our previous work with [^{89}Zr]Zr-DFO-huAR9.6 (*10*), we analyzed the behavior of [^{89}Zr]Zr-DFO-huAR9.6 in nude mice bearing OVCAR3, OVCAR4, OVCAR5, and OVCAR8 subcutaneous xenografts. Immuno-PET imaging showed high uptake of the radiotracer at 144 h after injection in OVCAR3 and OVCAR4 tumors, low uptake in OVCAR5 tumors, and minimal signal in OVCAR8 tumors (Fig. 1D). Biodistribution data at 144 h confirmed the uptake seen in the PET images, reaching approximately 35%, 30%, 13%, and 1% in OVCAR3, OVCAR4, OVCAR5, and OVCAR8 tumors, respectively (Fig. 1E; Supplemental Figs. 7–10). [^{89}Zr]Zr-DFO-huAR9.6 was also analyzed in R2G2 mice in preparation for therapy studies. R2G2 mice have a higher subcutaneous uptake rate by OC tumors than do nude mice and are more radioresistant than NSG mice (Jackson Laboratory). Biodistribution studies on R2G2 mice with [^{89}Zr]Zr-DFO-huAR9.6 confirmed significant tumor uptake by 72 h, which could be blocked with the addition of unlabeled huAR9.6 (Supplemental Fig. 11).

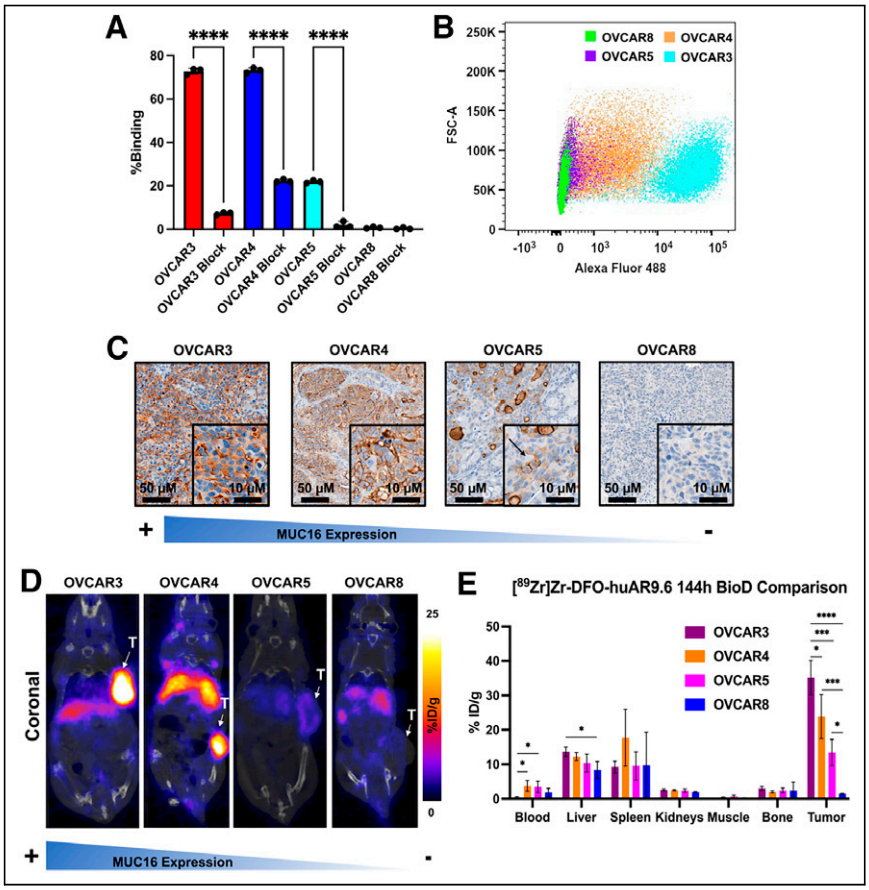

FIGURE 1. huAR9.6 can differentiate between OC cells with high and low MUC16 expression in vitro and in vivo. (A) Radioligand cell-binding assay with [^{89}Zr]Zr-DFO-huAR9.6 in cell lines with varying levels of MUC16 expression. Binding was significantly reduced with administration of 1,000-fold excess blocking dose of nonlabeled huAR9.6. (B) In vitro validation of huAR9.6-AF488 binding in OC cells via flow cytometry. (C) huAR9.6 immunohistochemical staining images of harvested OVCAR3, OVCAR4, OVCAR5, and OVCAR8 subcutaneous tumors. Arrow indicates MUC16 expression on surface of OVCAR5 cells. (D) Female nude mice containing subcutaneous tumors that were injected with 7.4–9.25 MBq (20–25 μg) of [^{89}Zr]Zr-DFO-huAR9.6 followed by PET imaging. (E) Terminal biodistributions at 144 h after injection. n = 3 for OVCAR4 and OVCAR8; n = 4 for OVCAR3 and OVCAR5. *$P \leq 0.05$. ***$P \leq 0.001$. ****$P \leq 0.0001$. %ID = percentage injected dose; FSC-A = forward scatter area; T = tumor.

[^{177}Lu]Lu-CHX-A″-DTPA-huAR9.6 Demonstrates Robust Antitumor Effects in OC Mouse Model

[^{177}Lu]Lu-CHX-A″-DTPA-huAR9.6 was synthesized at high radiochemical purity and was stable in human serum over 7 d (Supplemental Figs. 12, 13, 14A, and 14B). The radioimmunoconjugate maintained highly specific binding to the OVCAR3 cell line (Supplemental Figs. 14C and 15) and significant tumor uptake in the R2G2 model (Supplemental Fig. 16). A radioimmunotherapy study was performed on OVCAR3 tumor–bearing R2G2 mice. The mice were divided into 3 cohorts of [^{177}Lu]Lu-CHX-A″-DTPA-huAR9.6 with different specific activities: 9.25, 18.5, and 27.75 MBq. [^{177}Lu]Lu-CHX-A″-DTPA-huAR9.6 doses were confirmed by dosimetry estimates that were generated from xenografted OVCAR3 mouse biodistribution studies (Supplemental Fig. 17) (*24–28*). The dosimetry estimates indicated the appropriate dose to achieve tumor response while maintaining tolerable radiation exposure of healthy tissues (*29*,*30*). This study also included 2 control groups: saline and a 9.25-MBq [^{177}Lu]Lu-CHX-A″-DTPA-IgG isotype control. Overall survival in the 9.25- and 18.5-MBq cohorts was significantly higher than in the saline and IgG control groups (Fig. 2A). Potent antitumor effects were seen in all cohorts in comparison to control groups (Fig. 2B; Supplemental Fig. 18). All 5 mice in the 18.5-MBq cohort

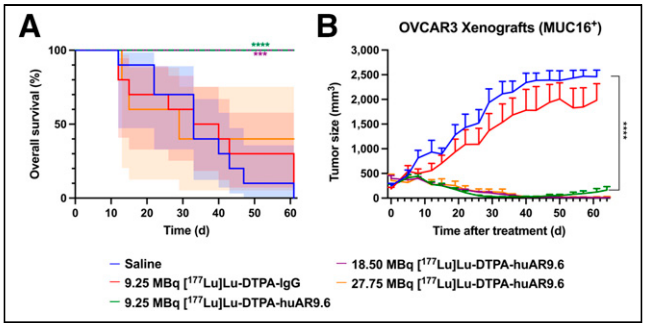

FIGURE 2. [^{177}Lu]Lu-CHX-A″-DTPA-huAR9.6 treatment improves overall survival and inhibits tumor growth in OVCAR3-bearing mice. (A and B) Overall survival percentage (A) and TV (mm^3) growth curves (B) of R2G2 OVCAR3-bearing mice after treatment. Significant tumor growth inhibition was observed in all treated mice in comparison to saline and IgG isotype controls. Shading represents 95% CI. ***$P \leq 0.001$. ****$P \leq 0.0001$.

and 2 of 5 mice in 27.75-MBq cohort had complete and durable responses after a single dose of [^{177}Lu]Lu-CHX-A″-DTPA-huAR9.6. Two mice in the 27.75-MBq group died of undetermined causes (days 13 and 15 after injection); however, these mice were experiencing decreases in body weight and blood cell counts before death. The third mouse was euthanized because it lost more than 20% of its initial body weight (day 29 after injection).

Nine of 15 tumors in the lowest-dose [^{177}Lu]Lu-CHX-A″-DTPA-huAR9.6 cohort demonstrated recurrence at an approximate range of 5–10 wk after treatment. Mouse 2 was not retreated, because it developed a severe skin infection, and mouse 12 was euthanized to harvest the tumor for analysis. Immunohistochemical analysis with huAR9.6 was performed to confirm maintenance of MUC16 expression (Supplemental Fig. 19). Three mice with recurrent tumors (mice *6–8*) were injected with [^{89}Zr]Zr-DFO-huAR9.6 (day 60 after treatment). PET/CT imaging confirmed MUC16 expression (Fig. 3A), suggesting the opportunity for retreatment with [^{177}Lu]Lu-CHX-A″-DTPA-huAR9.6. The mice received 9.25 MBq of [^{177}Lu]Lu-CHX-A″-DTPA-huAR9.6 (day 75 after initial treatment), which led to a complete response by approximately 6 wk after injection (Fig. 3B). The remaining 4 mice (mice *11* and *13–15*) with recurrent tumors were also injected with another 9.25-MBq dose of [^{177}Lu]Lu-CHX-A″-DTPA-huAR9.6 (day 121 after initial treatment), and uptake of the radiopharmaceutical was confirmed via SPECT/CT (Supplemental Fig. 20A). The tumors completely regressed by approximately 6 wk after retreatment (Supplemental Fig. 20B) but recurred at about 8 wk.

Additional radioimmunotherapy studies were performed on OVCAR5 (MUC16-positive/low) and OVCAR8 (MUC16-negative) xenografts. Both studies consisted of a group receiving a single 9.25-MBq dose of [^{177}Lu]Lu-CHX-A″-DTPA-huAR9.6, a saline control group, and a group receiving a single 9.25-MBq dose of [^{177}Lu]Lu-CHX-A″-DTPA-IgG. [^{177}Lu]Lu-CHX-A″-DTPA-huAR9.6 delayed tumor growth in the OVCAR5 xenografts in comparison to the saline control; however, this effect was not significant in comparison to the [^{177}Lu]Lu-CHX-A″-DTPA-IgG group (Supplemental Fig. 21A). This result is likely attributable to the low MUC16 expression of OVCAR5 tumors. In addition, the delayed tumor growth seen in the [^{177}Lu]Lu-CHX-A″-DTPA-IgG group was likely due to the enhanced permeability and retention effect, which allows for nonspecific accumulation in the tumor. Although the antitumor effect of [^{177}Lu]Lu-CHX-A″-DTPA-huAR9.6 was not significant in comparison to [^{177}Lu]Lu-CHX-A″-DTPA-IgG, mice in the treatment group showed improved overall survival in comparison to the saline control group, whereas the [^{177}Lu]Lu-CHX-A″-DTPA-IgG group did not show improved survival (Supplemental Figs. 21B and 22). No significant antitumor effects were seen in the OVCAR8 xenografts in comparison to controls, as expected from the lack of MUC16 expression in this model (Supplemental Fig. 23).

Hematologic Toxicity Is Transient in [^{177}Lu]Lu-CHX-A″-DTPA-huAR9.6–Treated Mice

Estimates of murine dosimetry implicated hematologic toxicity as the likely predominant radiogenic toxicity for radioimmunotherapy (Supplemental Fig. 17). To test the significance of hematologic toxicity, weekly blood analysis was implemented throughout the study in OVCAR3, OVCAR5, and OVCAR8 xenografts (Supplemental Figs. 24–26). The mean white blood cell, red blood cell, and platelet counts in OVCAR3 xenografts showed a dose-dependent decrease (Figs. 4A–4C). Platelet and white blood cell counts were most sensitive to radiation, but all cell counts recovered close to pretherapy levels or ranges after therapy initiation. Overall, hematologic toxicity was transient, with a nadir at 2–3 wk. Recovery to pretherapy values was achieved; that is, values recovered to ±1 SD of the average pretherapy values. To assess outward signs of toxicity, the mice were weighted twice weekly and monitored for observable symptoms, including changes in behavior and appearance. Significant weight loss was seen in 1 OVCAR3-bearing mouse in both the 18.5-MBq and the 27.75-MBq [^{177}Lu]Lu-CHX-A″-DTPA-huAR9.6 groups (Fig. 4D; Supplemental Fig. 27). Mice in the 27.75-MBq [^{177}Lu]Lu-CHX-A″-DTPA-huAR9.6 group demonstrated greater weight loss than mice in the lower-dose groups, indicating a dose-dependent toxicity response, with a nadir at about 2 wk. Mild petechia was also observed in the 27.75-MBq cohort. Similarly, weight loss was seen in OVCAR5 xenografts that received 9.25 MBq of [^{177}Lu]Lu-CHX-A″-DTPA-huAR9.6 or [^{177}Lu]Lu-CHX-A″-DTPA-IgG. However, average weight loss in those 2 groups did not exceed the 20% cutoff, with a nadir at about 2 wk (Supplemental Figs. 28 and 29).

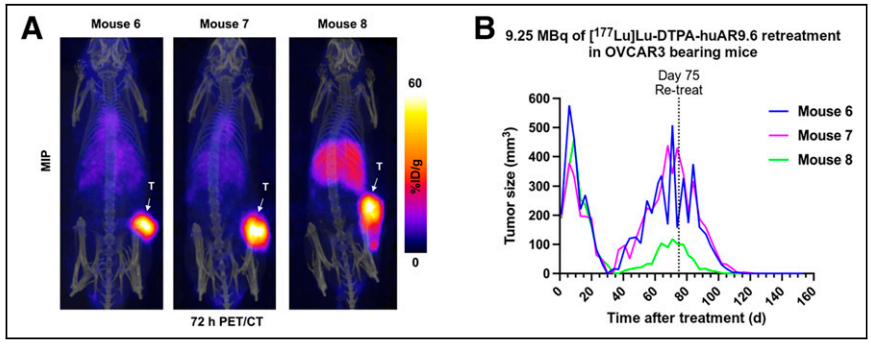

FIGURE 3. [^{177}Lu]Lu-CHX-A″-DTPA-huAR9.6 still shows strong antitumor effects in recurrent tumors. (A) 72-h PET/CT imaging with [^{89}Zr]Zr-DFO-huAR9.6 shows that OVCAR3 recurrent tumors still strongly express MUC16. Images are represented as maximum-intensity projections. (B) Individual TVs for recurrent OVCAR3 tumors. Mice were retreated with 9.25 MBq of [^{177}Lu]Lu-CHX-A″-DTPA-huAR9.6 at day 75 of therapy. %ID = percentage injected dose; MIP = maximum-intensity projection; T = tumor.

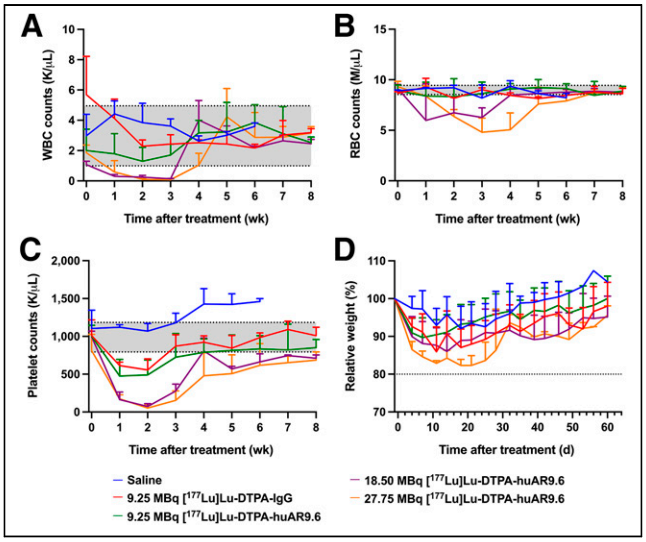

FIGURE 4. Hematologic toxicity is transient in [^{177}Lu]Lu-CHX-A″-DTPA-huAR9.6–treated mice with OVCAR3 tumors. (A–C) White blood cell counts (A), red blood cell counts (B), and platelet counts (C) in OVCAR3-bearing mice that received [^{177}Lu]Lu-CHX-A″-DTPA-huAR9.6 treatment. Shading indicates mean ± SD of values collected from entire cohort of OVCAR3-bearing mice before therapy initiation (week 0). (D) Mean relative weight percentages for OVCAR3-bearing mice in each cohort. RBC = red blood cell; WBC = white blood cell.

DISCUSSION

A theranostic approach integrates the diagnostic and therapeutic agent into a single platform (*31*). This method offers great potential to solve the challenges presented by late-stage diagnosis and poor therapeutic response. There is a critical need for earlier detection methods and additional precision-based therapies against novel targets for OC patients; therefore, we proposed the use of a radiotheranostic approach using huAR9.6.

huAR9.6 has a novel mechanism of action in comparison to other MUC16-targeting antibodies (*9*,*32*,*33*). In addition, huAR9.6 is a humanized antibody, allowing for higher tolerance and decreased immunogenicity in comparison to murine antibodies. We validated the diagnostic agent, [^{89}Zr]Zr-DFO-huAR9.6, in OC xenografts with varying MUC16 expression levels. Off-target uptake was identified within the liver and spleen, as may be attributed to MUC16 being a shed antigen, clearance of immunocomplexes by the reticuloendothelial system, or nonspecific binding of huAR9.6 to hepatic Fc receptors. In an OC patient study, the MUC16-targeting antibody (B43.13) showed binding to circulating MUC16 in the serum of patients, and the radioimmunoconjugate accumulated within the reticuloendothelial system (*34*,*35*). For our studies, serum levels of MUC16 were not detected via enzyme-linked immunosorbent assay. This can be attributed to a lack of high levels of MUC16 shed into the bloodstream in subcutaneous mouse models. Nonspecific binding to Fc receptors in the liver is common for radiolabeled full-length IgG antibodies because these antibodies still have an intact Fc region (*36*,*37*). Nonspecific uptake in these organs did not significantly affect tumor uptake; however, nonspecific uptake could potentially be blocked with the administration of an excess of unlabeled antibody before administration of its radiolabeled counterpart (*38*,*39*). Antibodies targeting shed antigen have been successfully used in the clinic for immuno-PET imaging with this approach (*40*).

Tumor uptake in OVCAR3, OVCAR5, and OVCAR8 xenografts correlated with [^{177}Lu]Lu-CHX-A″-DTPA-huAR9.6 therapy response. [^{177}Lu]Lu-CHX-A″-DTPA-huAR9.6 portrayed strong antitumor effects in all 3 tested doses in OVCAR3 xenografts. The maximum efficacious dose was 27.75 MBq; however, this dose did cause significant toxicity in 3 of the 5 mice. The 9.25- and 18.5-MBq [^{177}Lu]Lu-CHX-A″-DTPA-huAR9.6 cohorts experienced significantly improved overall survival in comparison to the saline control. Therapy with a single dose of [^{177}Lu]Lu-CHX-A″-DTPA-huAR9.6 did not have strong antitumor effects in OVCAR5 xenografts. It is possible that a single dose of [^{177}Lu]Lu-CHX-A″-DTPA-huAR9.6 is not sufficient to treat tumors with low MUC16 expression. Additional studies are warranted to investigate whether multiple doses would be beneficial in this model.

Tumor recurrence after a single low dose of [^{177}Lu]Lu-CHX-A″-DTPA-huAR9.6 did occur in a few OVCAR3-bearing mice. We hypothesized that a second administration of [^{177}Lu]Lu-CHX-A″-DTPA-huAR9.6 could be beneficial for retreating the recurrent tumors. The diagnostic agent, [^{89}Zr]Zr-DFO-huAR9.6, allowed us to predict whether the mice with recurrent tumors could benefit from a second administration of the radioimmunotherapy. Recurrent tumor burden was completely regressed with a second dose of [^{177}Lu]Lu-CHX-A″-DTPA-huAR9.6, indicating that multiple doses are beneficial for retreatment. However, tumor recurrence did occur about 60 d after the second dose in 2 of 7 retreated mice, and a third dose was not tested.

Radioimmunotherapy is often limited by hematologic toxicity due to slow clearance of the radiotracer from the blood (*41*). The treatment cohorts demonstrated dose-dependent toxicity, with the most severe reduction in platelet and white blood cell counts seen in the highest-dose cohort (27.75 MBq). However, hematologic effects from the radioimmunotherapy were transient, and blood counts rebounded over time.

CONCLUSION

The combination of the highly specific huAR9.6 antibody with a PET or therapeutic radionuclide allowed us to identify and treat tumors noninvasively. In this work, we validated the theranostic capability of [^{89}Zr]Zr-DFO-huAR9.6 in OC models. Furthermore, we demonstrated the strong antitumor effects of [^{177}Lu]Lu-CHX-A″-DTPA-huAR9.6 in highly MUC16-expressing tumors. These findings demonstrate great potential for using ^{89}Zr- and ^{177}Lu-labeled huAR9.6 as a theranostic pair for the identification and personalized treatment of MUC16-positive OC.

DISCLOSURE

The humanization of AR9.6 was funded by a private research contract to Cory Brooks from Quest Pharmatech Inc. during the conduct of the study. Jason Lewis reports grants from the NIH (R35 CA232130), Emerson Collective Cancer Research Fund, Tow Foundation, and IMRAS Memorial Sloan Kettering Cancer Center during this study. This study was also supported in part by the NIH R35 CA232130-S2 Diversity Supplement, awarded to Kyeara Mack. The Radiochemistry and Molecular Imaging Probes Core Facility, the Small Animal Imaging Facility, and the Molecular Cytology Core Facility were supported in part by NIH P30 CA08748. Prakash Radhakrishnan and Michael Hollingsworth acknowledge the NIH for support (CA208108 and P01CA217798). No other potential conflict of interest relevant to this article was reported.

ACKNOWLEDGMENTS

We gratefully acknowledge the support of the Radiochemistry and Molecular Imaging Probes Core Facility (Memorial Sloan Kettering), the Small Animal Imaging Facility (Memorial Sloan Kettering), and the Tri-Institutional Laboratory of Comparative Pathology. The Medical Graphics Department at Memorial Sloan Kettering Cancer Center is acknowledged. Dr. Sebastien Monette and Maria S. Jiao are gratefully acknowledged for assistance with ex vivo histopathologic examination. Quest Pharmatech is acknowledged for providing the AR9.6 antibody.

KEY POINTS

QUESTION: Can ^{89}Zr- and ^{177}Lu-labeled huAR9.6 be used as a theranostic platform for the diagnosis and treatment of OC?

PERTINENT FINDINGS: Hypoglycosylated MUC16 isoforms in OC can be detected via immuno-PET imaging with the MUC16-targeting radiotracer [^{89}Zr]Zr-DFO-huAR9.6. In vivo studies showed that [^{89}Zr]Zr-DFO-huAR9.6 could successfully delineate varying MUC16 expression levels in OC mouse models. Subsequent radioimmunotherapy studies with [^{177}Lu]Lu-CHX-A″-DTPA-huAR9.6 demonstrated improved overall survival and strong antitumor responses in highly MUC16-expressing models.

IMPLICATIONS FOR PATIENT CARE: Immuno-PET imaging of MUC16 with the huAR9.6 mAb may allow for noninvasive diagnosis and treatment monitoring of OC lesions in patients. This theranostic platform may be used to stratify and select patients who would benefit from the targeted radioimmunotherapy.

REFERENCES

1. Torre LA, Trabert B, DeSantis CE, et al. Ovarian cancer statistics, 2018. *CA Cancer J Clin.* 2018;68:284–296.
2. Special section: ovarian cancer. In: *Cancer Facts & Figures: 2018.* American Cancer Society; 2018:28–43.
3. Li SS, Ma J, Wong AST. Chemoresistance in ovarian cancer: exploiting cancer stem cell metabolism. *J Gynecol Oncol.* 2018;29:e32.
4. Scholler N, Urban N. CA125 in ovarian cancer. *Biomark Med.* 2007;1:513–523.
5. Radhakrishnan P, Dabelsteen S, Madsen FB, et al. Immature truncated O-glycophenotype of cancer directly induces oncogenic features. *Proc Natl Acad Sci USA.* 2014;111:E4066–E4075.
6. Akita K, Yoshida S, Ikehara Y, et al. Different levels of sialyl-Tn antigen expressed on MUC16 in patients with endometriosis and ovarian cancer. *Int J Gynecol Cancer.* 2012;22:531–538.
7. Kobayashi H, Terao T, Kawashima Y. Serum sialyl Tn antigen as a prognostic marker in patients with epithelial ovarian cancer. *Nippon Sanka Fujinka Gakkai Zasshi.* 1992;44:14–20.
8. Heskamp S, Raavé R, Boerman O, et al. ^{89}Zr-immuno-positron emission tomography in oncology: state-of-the-art ^{89}Zr radiochemistry. *Bioconjug Chem.* 2017;28:2211–2223.
9. Thomas D, Sagar S, Liu X, et al. Isoforms of MUC16 activate oncogenic signaling through EGF receptors to enhance the progression of pancreatic cancer. *Mol Ther.* 2021;29:1557–1571.
10. Sharma SK, Mack KN, Piersigilli A, et al. ImmunoPET of ovarian and pancreatic cancer with AR9.6, a novel MUC16-targeted therapeutic antibody. *Clin Cancer Res.* 2022;28:948–959.
11. Dash A, Pillai MR, Knapp FF Jr. Production of ^{177}Lu for targeted radionuclide therapy: available options. *Nucl Med Mol Imaging.* 2015;49:85–107.
12. Maughan TS, Haylock B, Hayward M, et al. OC125 immunoscintigraphy in ovarian carcinoma: a comparison with alternative methods of assessment. *Clin Oncol (R Coll Radiol).* 1990;2:199–205.
13. Papazefkos V, Michalas S, Papantoniou V, et al. Comparative study of RIS with the ^{131}I-OC 125 F(ab′)2 Mab and CT scan prior to second look operation for ovarian cancer. *Eur J Obstet Gynecol Reprod Biol.* 1990;37:271–277.
14. Perkins AC, Powell MC, Wastie ML, et al. A prospective evaluation of OC125 and magnetic resonance imaging in patients with ovarian carcinoma. *Eur J Nucl Med.* 1990;16:311–316.
15. Barzen G, Mayr AC, Langer M, et al. Radioimmunoscintigraphy of ovarian cancer with 131-iodine labeled OC-125 antibody fragments. *Eur J Nucl Med.* 1989;15:42–48.
16. Peltier P, Dutin JP, Chatal JF, et al. Usefulness of imaging ovarian cancer recurrence with In-111-labeled monoclonal antibody (OC 125) specific for CA 125 antigen. The INSERM Research Network (Nantes, Rennes, Reims, Vuillejuif, Saclay. *Ann Oncol.* 1993;4:307–311.
17. Vuillez JP, Levrot E, Mousseau M, et al. Evaluation of the diagnostic usefulness of CA125 immunoscintigraphy for ovarian carcinoma follow-up after treatment: contribution of this technique in Grenoble University Medical Center. *Bull Cancer.* 1997;84:1033–1042.
18. Finkler NJ, Muto MG, Kassis AI, et al. Intraperitoneal radiolabeled OC 125 in patients with advanced ovarian cancer. *Gynecol Oncol.* 1989;34:339–344.
19. Mahé MA, Fumoleau P, Fabbro M, et al. A phase II study of intraperitoneal radioimmunotherapy with iodine-131-labeled monoclonal antibody OC-125 in patients with residual ovarian carcinoma. *Clin Cancer Res.* 1999;5:3249s–3253s.
20. Muto MG, Finkler NJ, Kassis AI, et al. Human anti-murine antibody responses in ovarian cancer patients undergoing radioimmunotherapy with the murine monoclonal antibody OC-125. *Gynecol Oncol.* 1990;38:244–248.
21. Holland JP, Sheh Y, Lewis JS. Standardized methods for the production of high specific-activity zirconium-89. *Nucl Med Biol.* 2009;36:729–739.
22. Vosjan MJ, Perk LR, Visser GW, et al. Conjugation and radiolabeling of monoclonal antibodies with zirconium-89 for PET imaging using the bifunctional chelate p-isothiocyanatobenzyl-desferrioxamine. *Nat Protoc.* 2010;5:739–743.
23. Sharma SK, Lyashchenko SK, Park HA, et al. A rapid bead-based radioligand binding assay for the determination of target-binding fraction and quality control of radiopharmaceuticals. *Nucl Med Biol.* 2019;71:32–38.
24. Comuzzi C, Polese P, Melchior A, et al. SOLVERSTAT: a new utility for multipurpose analysis. An application to the investigation of dioxygenated Co(II) complex formation in dimethylsulfoxide solution. *Talanta.* 2003;59:67–80.
25. Bolch WE, Eckerman KF, Sgouros G, et al. MIRD pamphlet no. 21: a generalized schema for radiopharmaceutical dosimetry—standardization of nomenclature. *J Nucl Med.* 2009;50:477–484.
26. Carter LM, Crawford TM, Sato T, et al. PARaDIM: A PHITS-based Monte Carlo tool for internal dosimetry with tetrahedral mesh computational phantoms. *J Nucl Med.* 2019;60:1802–1811.
27. Sato T, Niita K, Matsuda N, et al. Overview of particle and heavy ion transport code system PHITS. *Ann Nucl Energy.* 2015;82:110–115.
28. Kesner A, Olguin E, Zanzonico P, et al. MIRDCalc V 1.0: a community spreadsheet tool for organ-level radiopharmaceutical absorbed dose calculations [abstract]. *J Nucl Med.* 2018;59(suppl 1):473.
29. Larson SM, Carrasquillo JA, Cheung NK, Press OW. Radioimmunotherapy of human tumours. *Nat Rev Cancer.* 2015;15:347–360.
30. Emami B, Lyman J, Brown A, et al. Tolerance of normal tissue to therapeutic irradiation. *Int J Radiat Oncol Biol Phys.* 1991;21:109–122.
31. Bodei L, Herrmann K, Schöder H, et al. Radiotheranostics in oncology: current challenges and emerging opportunities. *Nat Rev Clin Oncol.* 2022;19:534–550.
32. Nemieboka B, Sharma SK, Rao TD, et al. Radiopharmacologic screening of antibodies to the unshed ectodomain of MUC16 in ovarian cancer identifies a lead candidate for clinical translation. *Nucl Med Biol.* 2020;86-87:9–19.
33. Sharma SK, Wuest M, Wang M, et al. Immuno-PET of epithelial ovarian cancer: harnessing the potential of CA125 for non-invasive imaging. *EJNMMI Res.* 2014;4:60.
34. McQuarrie SA, Baum RP, Niesen A, et al. Pharmacokinetics and radiation dosimetry of ^{99}Tc^{m}-labelled monoclonal antibody B43.13 in ovarian cancer patients. *Nucl Med Commun.* 1997;18:878–886.
35. McQuarrie SA, Riauka T, Baum RP, et al. The effects of circulating antigen on the pharmacokinetics and radioimmunoscintigraphic properties of ^{99m}Tc labelled monoclonal antibodies in cancer patients. *J Pharm Pharm Sci.* 1998;1:115–125.
36. Boyle CC, Paine AJ, Mather SJ. The mechanism of hepatic uptake of a radiolabelled monoclonal antibody. *Int J Cancer.* 1992;50:912–917.
37. Hosseinimehr SJ, Tolmachev V, Orlova A. Liver uptake of radiolabeled targeting proteins and peptides: considerations for targeting peptide conjugate design. *Drug Discov Today.* 2012;17:1224–1232.
38. Houghton JL, Abdel-Atti D, Scholz WW, Lewis JS. Preloading with unlabeled CA19.9 targeted human monoclonal antibody leads to improved PET imaging with ^{89}Zr-5B1. *Mol Pharm.* 2017;14:908–915.
39. Henry KE, Shaffer TM, Mack KN, et al. Exploiting the MUC5AC antigen for noninvasive identification of pancreatic cancer. *J Nucl Med.* 2021;62:1384–1390.
40. Lohrmann C, O'Reilly EM, O'Donoghue JA, et al. Retooling a blood-based biomarker: phase I assessment of the high-affinity CA19-9 antibody HuMab-5B1 for immuno-PET imaging of pancreatic cancer. *Clin Cancer Res.* 2019;25:7014–7023.
41. Sharkey RM, Goldenberg DM. Cancer radioimmunotherapy. *Immunotherapy.* 2011;3:349–370.